


Saturated Stimulated-Raman-Scattering Microscopy for Far-Field Superresolution Vibrational Imaging

Li Gong, Wei Zheng, Ying Ma, and Zhiwei Huang*

Optical Bioimaging Laboratory, Department of Biomedical Engineering, Faculty of Engineering, National University of Singapore, Singapore 117576

 (Received 1 October 2018; revised manuscript received 17 January 2019; published 18 March 2019)

Stimulated Raman-scattering (SRS) microscopy has emerged as a powerful tool for quantitative vibrational imaging of live tissues and cells with biochemical specificity, but the spatial resolution of SRS microscopy is still diffraction limited. We present work on saturated stimulated-Raman-scattering (SSRS) microscopy to break the diffraction limit for far-field superresolution imaging in biological systems. A virtual sinusoidal modulation (VSM) method is also proposed for retrieval of superresolution SSRS images. We show an experimental implementation of SSRS microscopy for enhancing the spatial resolution of SRS imaging in samples (e.g., plant cells, live HeLa cells) with a spectral focusing hyperspectral SRS system. With saturation occurring in coherent Raman processes under a certain level of excitation powers, it is anticipated that the SSRS technique has the ability to become an appealing tool for label-free far-field superresolution SRS imaging in biological and biomedical systems.

DOI: [10.1103/PhysRevApplied.11.034041](https://doi.org/10.1103/PhysRevApplied.11.034041)

I. INTRODUCTION

To break the diffraction limit for biological imaging, a variety of superresolution microscopy techniques based on fluorescent labeling have been developed in the past two decades, such as stimulated emission depletion (STED) microscopy [1], stochastic optical reconstruction microscopy (STORM) [2], photo-activated localization microscopy (PALM) [3], structured illumination microscopy (SIM) [4], and saturation excitation (SAX) microscopy [5]. Compared to fluorescence-based microscopy, coherent Raman-scattering microscopy [e.g., coherent anti-Stokes Raman scattering (CARS), stimulated Raman scattering (SRS)] utilizing the inherent chemical vibrational bonds as imaging contrast has been emerging as an appealing tool for label-free biomolecular imaging in biological and biomedical systems [6–11]. SRS microscopy associated with bio-orthogonal Raman tags (e.g., nitrile, alkyne and polyynes, etc.) [12,13] has also been explored for high-contrast quantitative imaging and supermultiplex in living cells. In both CARS and SRS microscopy, a pump beam (ω_p) and a Stokes beam ($\omega_s < \omega_p$) are tightly focused into the sample. Coherent Raman resonance happens when $\omega_p - \omega_s$ matches the frequency of a Raman-active vibrational mode along the phase-matching direction. CARS detects the output at a new frequency at $2\omega_p - \omega_s$, whereas SRS detects either the loss of the pump beam [called the stimulated Raman loss (SRL)] or the gain of the Stokes beam [called the stimulated

Raman gain (SRG)]. Compared to CARS, SRS microscopy is free of nonresonant background and is suitable for high-contrast vibrational bioimaging [7]. However, the spatial resolution of conventional CARS and SRS microscopy is still diffraction limited. Superresolution CARS and SRS microscopy would be very attractive for imaging live cells and even thick tissues, as coherent Raman-scattering techniques with near-infrared (NIR) excitations can have a larger penetration depth in biomedical systems [7]. Recent studies show that suppressing CARS and SRS signals may be a way to break the diffraction limit by using a STED-like scheme [14–16]. For instance, the SRS signal can be suppressed by adding a decoherence beam into a SRS system for improving the spatial resolution by up to a factor of two [17]. SRS and CARS may also be suppressed by introducing an additional competing SRS process for enhancing the spatial resolution [18–20]. Superresolution CARS microscopy with saturation is demonstrated in diamond crystal [21]. Focal volume engineering may be used to improve the lateral resolution by twofold although the axial resolution is sacrificed [22,23]. Supercritical focusing CARS has been reported for enhancing both axial and lateral resolutions [24]. SRS microscopy with excitation wavelengths in the visible range has been used for high-resolution bioimaging [25], although it is still diffraction limited.

Here, we propose and implement a far-field superresolution imaging scheme based on saturated stimulated-Raman-scattering (SSRS) processes. We experimentally demonstrate the SSRS scheme and also elucidate the SSRS results with theoretical modeling. A virtual sinusoidal

*biehzw@nus.edu.sg

modulation (VSM) method is also proposed to extract a superresolution SSRS image through a stack of SRS images under different excitation powers with different levels of saturation. We show an experimental implementation of SSRS microscopy for enhancing the spatial resolution of SRS imaging in the samples [e.g., 1,4-diphenylbuta-1,3-diene (DPBD) crystal, plant cells, live HeLa cells] with a spectral focusing hyperspectral SRS system [26]. With the saturation occurring in coherent Raman processes under a certain level of excitation powers, we expect that the SSRS technique has the ability to become an appealing tool for label-free far-field superresolution SRS imaging in biological and biomedical systems.

II. METHODS AND MATERIALS

A. Principle of SSRS process

Figure 1(a) shows the energy level diagram to study the saturation of SRS. Typically, a Raman process involves a ground state $|g\rangle$, a vibrational state $|v\rangle$, and an electronic state $|e\rangle$ [27]. In a real molecular system under intense pulse laser excitations, the overtone states above the vibrational state (labeled as $|v1\rangle$, $|v2\rangle$, etc.) can also be involved in molecular transitions via nonlinear optical processes [28]. For instance, if increasing the excitation power to excite a significant portion of molecules to $|v\rangle$, the subsequent transitions from $|v\rangle$ to overtone states may happen in a cascade manner. This makes the SRS process difficult to saturate and hence, the overtone states cannot be neglected in saturation of SRS. The status of the molecule can be represented by the density matrix $\rho = |\Psi\rangle\langle\Psi|$. The light-matter interaction is described semiclassically by the Liouville-von Neumann equation with phenomenological decay terms [27]

$$\begin{aligned} \frac{\partial \rho_{nm}}{\partial t} &= -i\omega_{nm}\rho_{nm} - \frac{i}{\hbar}[\hat{H}_{\text{int}}, \hat{\rho}]_{nm} - \gamma_{nm}\rho_{nm} \quad (n \neq m), \\ \frac{\partial \rho_{nn}}{\partial t} &= -\frac{i}{\hbar}[\hat{H}_{\text{int}}, \hat{\rho}]_{nn} + \sum_{E_m > E_n} \Gamma_{nm}\rho_{mm} - \sum_{E_m < E_n} \Gamma_{mn}\rho_{nn}, \end{aligned} \quad (1)$$

where $m, n = g, e, v, v1, v2, \dots$, and $\omega_{nm} = \omega_n - \omega_m$ is the frequency difference between the two states. γ_{nm} and Γ_{nm} are the decoherent rate and the delay rate, respectively. $\hat{H}_{\text{int}} = \hat{\mu} \cdot \mathbf{E}$ is the interaction Hamiltonian determining the strength of light-matter interaction, in which $\hat{\mu}$ is the electronic dipole momentum operator and \mathbf{E} is the electric field of the incident light with a Gaussian temporal profile [14,16]

$$\mathbf{E} = [\mathbf{A}_p \cos(\omega_p t) + \mathbf{A}_S \cos(\omega_S t)] \exp[-2 \ln 2 (t - t_0)^2 / \tau^2], \quad (2)$$

where \mathbf{A}_p and \mathbf{A}_S are the field amplitudes of the pump and Stokes beams, respectively. τ is the pulsewidth of

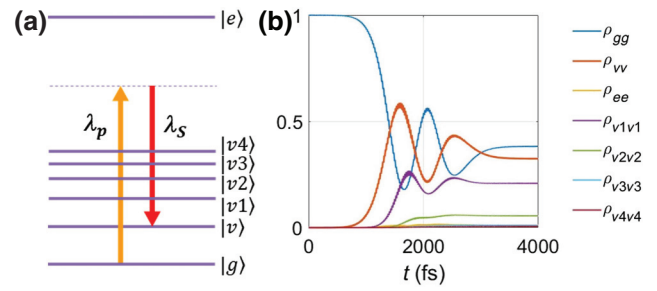


FIG. 1. Principle of SRS processes. (a) Energy-level diagram of SRS. (b) Temporal evolution of molecules populated in different energy levels ($\lambda_{eg} = 500$ nm, $\tau = 2$ ps, and $\Omega_p = \Omega_S = 200$ THz).

both pump and Stokes pulses in terms of the FWHM of intensity.

Here, the Raman shift is set to be $\Delta k_{vg} = 1500$ cm^{-1} . The pump wavelength is set to be $\lambda_p = 800$ nm, such that λ_S should be 909.1 nm to match the Raman shift. Two cases for the pulsewidths ($\tau = 2$ ps and $\tau = 100$ fs) are considered for modeling, since both ps and fs lasers are typically used in SRS imaging. For the electronic state, since the electronic absorption of common biological samples spans from ultraviolet (UV) to visible regions, three cases will be considered: that is, the wavelengths of the transition from $|g\rangle$ to $|e\rangle$ are $\lambda_{eg} = 300$ nm (off-resonant excitation), 500 nm (off-resonant excitation), and 650 nm (preresonant excitation). (Details of other parameters refer to Sec. I of the Supplemental Material [29] and Refs. [14–16,27,30–36].) Equation (1) can be solved numerically by using the Runge-Kutta algorithm of the fourth order from 0 to 4 ps (the center of the pulse is at $t_0 = 2$ ps) to obtain the temporal evolution of population on each molecular level for each set of parameters. Figure 1(b) shows an example of the modeling results ($\lambda_{eg} = 500$ nm, $\tau = 2$ ps, and $\Omega_p = \Omega_S = 200$ THz). Instead of using the peak intensities I_p and I_S , the peak Rabi frequencies for both pump ($\Omega_p = \mu_{eg} \cdot \mathbf{E}_p / \hbar \propto \sqrt{I_p}$) and Stokes ($\Omega_S = \mu_{eg} \cdot \mathbf{E}_S / \hbar \propto \sqrt{I_S}$) beams are used, hence our results in Fig. 1(b) are generic for different dipole momenta of the molecule and different polarizations of light. Initially, due to the $|g\rangle \rightarrow |v\rangle$ transition induced by a conventional SRS process, the population on the vibrational state ρ_{vv} starts to increase, while the population on the ground state ρ_{gg} starts to decrease from 1. Subsequently, the populations on the first and the second overtone states (ρ_{v1v1} and ρ_{v2v2}) start to increase in sequence due to the cascaded transitions $|v\rangle \rightarrow |v1\rangle$ and $|v1\rangle \rightarrow |v2\rangle$. In the entire light-molecule-interaction period, both ρ_{v3v3} and ρ_{v4v4} are $\ll 1$, thus it suffices to include the first four overtone states for SSRS simulations. One notes that in SRL and SRG measurements, the cascaded transitions contributing to the SRS signal cannot be distinguished from a conventional SRS

process and hence, the overtone states have to be considered in the study of the saturation of SRS. Since $\rho_{ee} \ll 1$, most of the energy absorbed by the molecule is in vibrational states rather than in the electronic state. The populations on the ground state and all the vibrational states undergo Rabi oscillations with frequencies close to the two-photon Rabi frequency at 18 THz (period of approximately 350 fs) according to perturbation calculation of the Liouville-von Neumann equation in Ref. [16].

Figure 1(b) shows that at the time point $t = 4$ ps, the light-matter interaction is almost finished. Hence, we can estimate the energy transferred to the vibrational levels (including overtone states) and the electronic level as follows:

$$E_{\text{vib}} = \rho_{vv}|_{t=4\text{ ps}} \hbar\omega_{vg} + \sum_{i=1}^4 \rho_{vivi}|_{t=4\text{ ps}} \hbar\omega_{vig}, \quad (3)$$

$$E_{\text{ele}} = \rho_{ee}|_{t=4\text{ ps}} \hbar\omega_{eg}.$$

On one hand, the energy transferred to the vibrational states is mainly due to the SRS process [15,37]; on the other hand, while a pump photon is annihilated, a Stokes photon will be created. Therefore, $E_{\text{vib}}/(\hbar\omega_p - \hbar\omega_s)$ is the number of annihilated pump photons (or created Stokes photons) per molecule through the SRS process. This quantity is the SRS signal plotted in Figs. 2(a)–2(d). Similarly, the energy transferred to the electronic state arises from a multiphoton absorption (MPA) process. SRS cannot be distinguished from MPA, which becomes an unwanted background in SRS imaging. Assuming that the numbers of annihilated photons for both pump and Stokes are equal in MPA, the number of pump photons lost per molecule due to the presence of Stokes photons in MPA is $E_{\text{ele}}/(\hbar\omega_p + \hbar\omega_s)/2$.

The signal level of SRS can be calculated as a function of peak intensities. Figures 2(a) and 2(b) show two examples of SRS signal vs Rabi frequencies of pump and Stokes beams (Ω_p and Ω_s) in logarithmic scales, whereby $\lambda_{eg} = 500$ nm and the pulsewidths τ are 100 fs and 2 ps, respectively. This shows that the SRS signal can be saturated by both fs and ps lasers. Under saturation, the SRS signal is still roughly a function of the product of Ω_p and Ω_s . To more clearly visualize the saturation of SRS processes, Figs. 2(c) and 2(d) display SRS signals as a function of Ω ($\Omega = \Omega_p = \Omega_s$), as well as the populations on the vibrational state (vib) and the total population on overtone states (ovt) after the light-matter interaction. Obviously, when Ω is small [e.g., $\Omega < 300$ THz and $\Omega < 50$ THz in Figs. 2(c) and 2(d), respectively], the slope of SRS is 4, that is, $\text{SRS} \propto \Omega^4 \propto I_p I_s$. It is just a conventional (unsaturated) SRS process, and the populations on overtone states (ovt) are orders of magnitude smaller than that on the vibrational state (vib). But when Ω becomes larger, the population on the vibrational state reaches its maximum, while the population on overtone states gradually becomes comparable

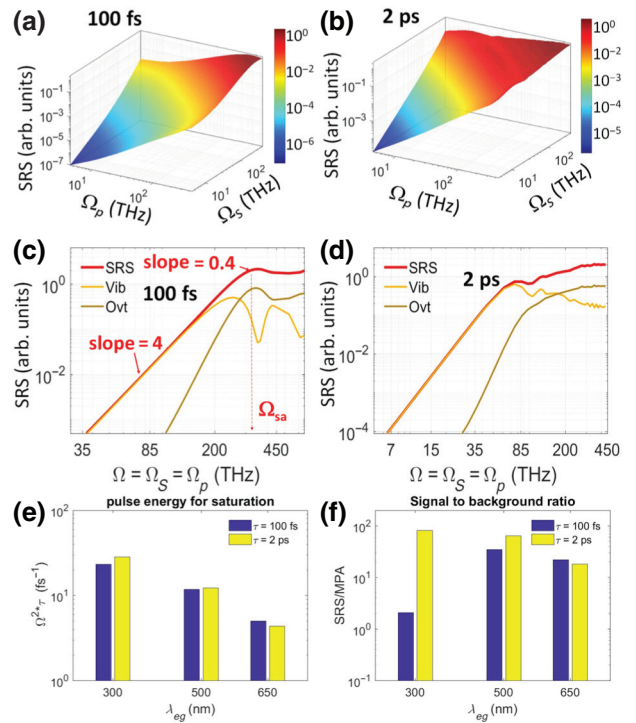


FIG. 2. Principle of saturation of SRS processes. (a),(b) The SRS signal as a function of Ω_p and Ω_s , for $\lambda_{eg} = 500$ nm, $\tau = 100$ fs, and for $\lambda_{eg} = 500$ nm, $\tau = 2$ ps, respectively. (c),(d) SRS, the population on the vibrational state (vib) and the total population on overtone states (ovt) after light-matter interaction as a function of peak Rabi frequency Ω ($\Omega_p = \Omega_s$), for $\lambda_{eg} = 500$ nm, $\tau = 100$ fs, and for $\lambda_{eg} = 500$ nm, $\tau = 2$ ps, respectively. The definition of the saturation Rabi frequency Ω_{sa} is illustrated in (c). Pulse energy (e) and SRS signal to MPA background ratio (f) for different sets of parameters under SRS saturation.

to that on the vibrational state and can still increase due to cascaded transitions [Figs. 2(c) and 2(d)].

According to Eq. (3), the excitations to both the vibrational state and overtone states contribute to SRS signal, thus the cascaded transitions to overtone states increase the SRS signal and reduce the saturation of the SRS process. The Raman shift of the cascaded transition from $|v\rangle$ to $|v1\rangle$ is 1465 cm^{-1} , which is 35 cm^{-1} less than the Raman shift from $|g\rangle$ to $|v\rangle$ (1500 cm^{-1}). For 2-ps-laser excitation, the spectrum resolution is 10.38 cm^{-1} , so that the cascaded Raman process is slightly off resonance; for 100-fs-laser excitation, the spectrum resolution is 207.6 cm^{-1} and the cascaded transition is within the spectrum resolution. Obviously, by comparing Figs. 2(c) and 2(d), the overtone states are much easier to be excited under fs laser excitation. Nevertheless, in both fs and ps excitation cases, although the cascaded transitions to overtone states may reduce saturation to a certain extent, they cannot fully stop SRS saturation.

For a better quantitative understanding of the saturation of SRS, we define a saturation Rabi frequency Ω_{sa} , whereby if a Rabi frequency is above the saturation Rabi frequency ($\Omega > \Omega_{sa}$), obvious saturation of the SRS processes will occur. Since saturation of SRS is a gradual process (i.e., the slope of SRS is gradually decreasing from 4 down to smaller values), Ω_{sa} can be defined as the Rabi frequency, bringing the slope of SRS down to 0.4 [a 90% decrease, as indicated in Fig. 2(c)].

In Fig. 2(e), $\Omega_{sa}^2 \tau$ is a quantity proportional to the pulse energy. When λ_{eg} is closer to λ_p (closer to the preresonant condition), the pulse energy required for saturation is apparently smaller. However, SRS is saturated under almost the same pulse energy for both ps and fs excitation. This may be due to the two competing processes involved in SRS transitions: (i) SRS is a third-order nonlinear optical process; saturation means that nonlinear optical processes higher than the third order are involved. In this regard, for the same pulse energy, the fs laser should be better for saturation due to its higher peak power. (ii) However, the fs laser is easier to excite the overtone states, thus it is more difficult to achieve saturation as compared to ps excitation. These two factors may compete and eventually almost cancel each other out, resulting in saturation of the SRS processes occurring under a similar pulse energy excitation with ps and fs lasers.

The signal-to-background ratios (i.e., SRS ratio to MPA) under saturation for both ps and fs excitations are shown in Fig. 2(f). Overall, SRS is an order of magnitude stronger than the MPA process for both ps and fs excitations. For the off-resonant excitation cases ($\lambda_{eg} = 300$ nm and $\lambda_{eg} = 500$ nm), the signal-to-background ratio is lower under fs excitation. If close to the preresonant excitation ($\lambda_{eg} = 650$ nm), the signal-to-background ratio becomes similar under fs and ps excitations. One notes that if λ_{eg} is shorter, higher-order MPA is involved (e.g., if $\lambda_{eg} = 300$ nm, MPA should be mainly due to three-photon absorption, while $\lambda_{eg} = 650$ nm can be reached by two-photon absorption). On the other hand, fs excitation, which has higher peak power, is more efficient for higher-order MPA than ps excitation with the same average power. Hence, the shorter λ_{eg} is used and the higher background can be generated by fs excitation.

One of the key tasks of our theoretical study on SSRS processes in this work is to quantitatively predict the excitation powers required for saturation of SRS processes in the samples. The saturation Rabi frequency Ω_{sa} can be calculated for each parameter set. Then, the peak intensity required to reach such a Rabi frequency can be calculated by $I_{sa} = 1/2c\epsilon_0[\Omega_{sa}\hbar/(\mu_{eg}/2)]^2$. For example, C-H stretching of biomolecules (e.g., proteins, lipids) is the most common Raman-active mode used in SRS imaging in biological systems. μ of C-H stretching is about 0.03 elementary charge times nanometer [16] and its λ_{eg} is around 200 nm [16], thus the peak intensity needed for

saturation will be about 1 TW/cm² or 15 TW/cm² for 2-ps or 100-fs lasers, respectively. The saturation peak intensities of our synthesized Raman tag required for superresolution SRS imaging are also calculated and compared with experimental results [Figs. 5(a) and 5(c)].

B. Virtual sinusoidal modulation method for superresolution SSRS imaging

The working principle of the VSM method is illustrated in Fig. 3 by using simulation results (Sec. II of the Supplemental Material for details [29]). As shown in Fig. 3(a), a stack of SRS images (e.g., SRL detected) is recorded

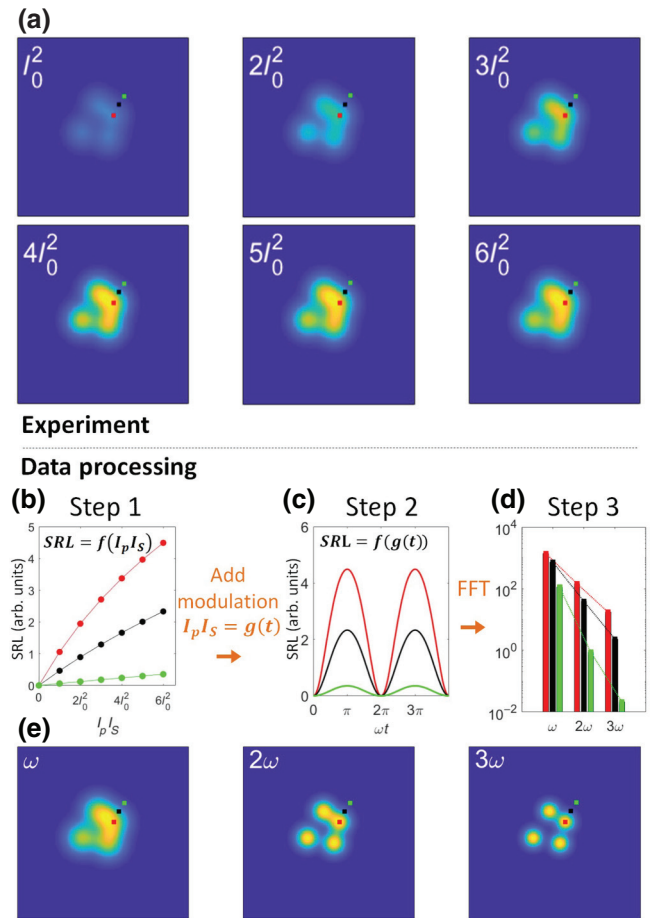


FIG. 3. Illustration of the VSM method for superresolution SSRS imaging. (a) SRS images under excitation intensity product $I_p I_s$ from I_0^2 to $6I_0^2$. (b) SRL vs $I_p I_s$ for selected pixels labeled in (a). The measured data points (round dots) and the linear interpolation (solid lines between data points) form the function $SRL = f(I_p I_s)$. (c) Assuming that $I_p I_s$ is sinusoidally modulated as $I_p I_s = g(t) = 6I_0^2 \times [\sin(\omega t) + 1]/2$, SRL should be modulated accordingly as $SRL = f[g(t)]$. (d) The Fourier transform of $SRL = f[g(t)]$. (e) The n th-order SSRS image can be retrieved by plotting the Fourier components of the n th harmonic order ($n\omega$) of all pixels as one image for which the resolution is enhanced by a factor of about \sqrt{n} .

under different excitation intensity products ($I_p I_S$ is from I_0^2 to $6I_0^2$), resulting in different levels of saturation. Then, the superresolution SSRS images will be retrieved by postprocessing of SRS images acquired with the following three steps:

Step 1 [Fig. 3(b)] to obtain the function SRL = $f(I_p I_S)$: From experimental data, for each pixel, we have several data points for SRL vs $I_p I_S$. Three examples [pixels labeled in red, black, and green in Fig. 3(a)] are shown in Fig. 3(b) as round dots. In principle, SRL is a function of $I_p I_S$, that is, $\text{SRL} = f(I_p I_S)$. These experiments only give several data points of this function. The missing data is added by linear interpolation [solid lines between data points in Fig. 3(b)]. It can be found that there is almost no saturation in the green pixel, a little saturation in the black pixel, and obvious saturation in the red pixel.

Step 2 [Fig. 3(c)] to apply modulation: Assuming that the excitation intensity product is modulated sinusoidally in the time domain as $I_p I_S = g(t) = 6I_0^2 \times [\sin(\omega t) + 1]/2$, we substitute $I_p I_S = g(t)$ into the relation $\text{SRL} = f(I_p I_S)$ to obtain a curve $\text{SRL} = f[g(t)]$.

Step 3 [Fig. 3(d)], Fourier transform: In Fourier space, different frequency components of the modulated signals $\{\text{SRL} = f[g(t)]\}$ are plotted in Fig. 3(d). If there is no saturation, that is, $\text{SRL} \propto I_p I_S$, $\text{SRL} = f[g(t)]$ should be sinusoidally modulated as well. Otherwise, $\text{SRL} = f[g(t)]$ becomes a distorted sinusoidal function, which contains higher-order harmonics. Therefore, higher-order harmonics can be utilized to distinguish different levels of saturation. The signal from the center of the laser foci is easier to saturate, thus such a signal can be distinguished from the signal generated by the outer parts of the laser foci, resulting in a better spatial resolution.

Finally, the n th-order SSRS image can be retrieved by plotting the Fourier components of the n th harmonic order ($n\omega$) of all pixels as one image, as shown in Fig. 3(e). Similar to fluorescence-labeled SAX microscopy [5], in principle, the spatial resolution of the n th harmonic order of SSRS imaging is enhanced by a factor of about \sqrt{n} [38].

Figure 4 shows a comparison between the VSM and SAX methods (Sec. II of the Supplemental Material for details [29]). The VSM method is essentially an alternative option of sinusoidal modulation in SAX. As long as enough data points are collected in VSM, the results should converge to SAX. Figure 4(a) plots the accuracy of the VSM method compared with SAX for retrieving different harmonic orders with different numbers of data points by linear sampling of $I_p I_S$, that is, for n data points, $I_p I_S = (1, 2, 3, \dots, n) \times \max(I_p I_S)/n$. Accuracy means how close the VSM result is to SAX, where an accuracy = 1 means perfect matching. It shows that n data points are enough to retrieve the harmonic order $n\omega$ when $n \leq 4$. This agrees with the Nyquist sampling theorem. However, if $n > 4$,

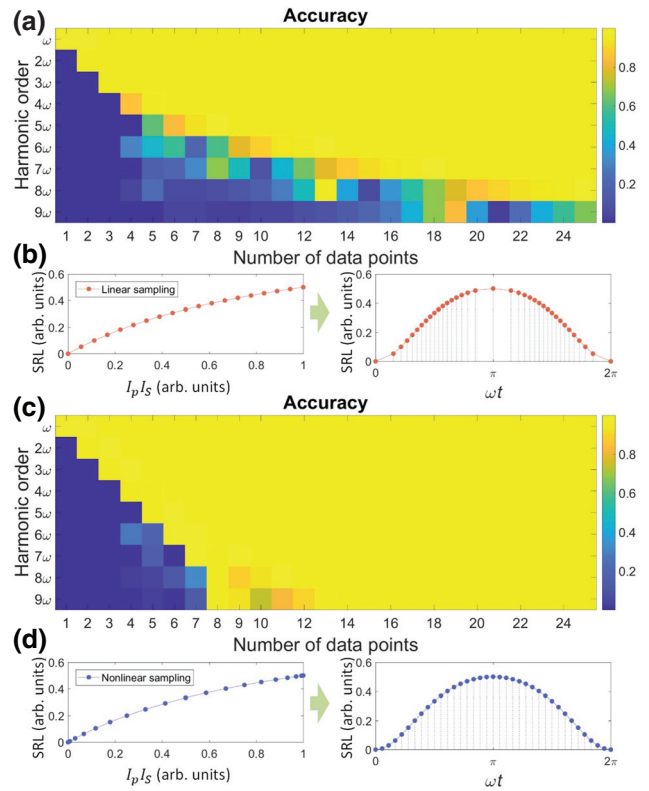


FIG. 4. Accuracy of the VSM method compared with SAX for retrieving different harmonic orders with different numbers of data points, by (a) linear sampling of $I_p I_S$ and (c) nonlinear sampling of $I_p I_S$. (b),(d), the strategy of linear and nonlinear sampling of $I_p I_S$.

more than n data points are needed to retrieve the information at $n\omega$. The reason for this is illustrated in Fig. 4(b), where a linear increase of $I_p I_S$ leads to a nonuniform sampling rate int , and this effect is more serious for largern. As shown in Fig. 4(c), this problem can be solved by nonlinear sampling of $I_p I_S$. Figure 4(d) illustrates nonlinear sampling as $I_p I_S = \max(I_p I_S) \times \{1 - \cos[\theta(\pi/n)]\}/2$, where $\theta = 1, 2, 3, \dots, n$, to keep a uniform sampling rate in t . Nevertheless, nonlinear sampling needs more data points at higher intensity, thus it is easier to damage the sample. Therefore, linear sampling is enough for low harmonic orders.

C. Materials

Details of synthesis of DPBD and triphenylphosphonium Buta-1,3-diyne-1,4- diylbis(4,1-phenylene) (TPP-BDBPD) and their properties are described in Sec. III of the Supplemental Material [29].

D. Cell culture and incubation

HeLa cells are cultured in Dulbecco's modified eagle medium (DMEM) containing high glucose, glutamax, and 10% fetal bovine serum. Cells are subcultured and plated

on a glass coverslip two days before imaging. For the mitochondria imaging, 3 μ l of TPP-BDBPD (0.2 mM in dimethyl sulfoxide) solution is injected into a well plate containing a glass coverslip and 3 ml of DMEM media, then the plate is immediately shaken to ensure a homogeneous solution. The cells are then incubated at 37 °C, 5% CO₂ for 20 min. After thoroughly washing with phosphate buffer solution three times, SRS imaging of HeLa cells is conducted.

E. Image acquisition parameters

The SRS image of a DPBD crystal in the x - y plane [Fig. 6(a)] is acquired with a pixel dwell time of 0.4 μ s and a pixel size of 75 nm, no average, $I_p = 284$ GW/cm², $I_S = 71.5$ GW/cm². The SSRS image [Fig. 6(c)] is retrieved by using the VSM method from four SRS images recorded with I_S increasing from 35.7 to 143 GW/cm² at intervals of 35.7 GW/cm², while I_p is kept constant at 284 GW/cm².

The SRS image of a DPBD crystal in the x - z plane [Fig. 6(h)] is acquired with a pixel dwell time of 0.4 μ s, a lateral pixel size of 158 nm, and an axial pixel size of 300 nm, no average, $I_p = 208$ GW/cm², $I_S = 29.5$ GW/cm². The SSRS image [Fig. 6(j)] is retrieved via VSM from five SRS images recorded with I_S increasing from 29.5 to 148 GW/cm² at an interval of 29.5 GW/cm², while I_p is kept constant at 208 GW/cm².

The SRS image of chloroplast in plant cells [Fig. 7(a)] is acquired with a pixel dwell time of 0.4 μ s and a pixel size of 79 nm, no average, $I_p = 182$ GW/cm², $I_S = 36.9$ GW/cm². The SSRS image [Fig. 7(b)] is retrieved from four SRS images recorded with I_S increasing from 36.9 to 148 GW/cm² by a step size of 36.9 GW/cm², while I_p is kept constant at 182 GW/cm².

The SRS image of mitochondria labeled with TPP-BDBPD in live HeLa cells [Fig. 7(f)] is acquired with a pixel dwell time of 2 μ s and a pixel size of 150 nm, averaged 40 times, $I_p = 70.9$ GW/cm², $I_S = 214$ GW/cm². The SSRS image [Fig. 7(g)] is retrieved from two SRS images recorded with I_p at 70.9 and 227 GW/cm², while I_S is kept constant at 214 GW/cm².

The pixel dwell time and pixel size of all the SSRS images are the same as their corresponding SRS images. For the images of the DPBD crystal in the x - y plane and the mitochondria, the objective used is Apo LWD 25X/1.10w, Nikon.

III. RESULTS

A. Experimental observation of saturation of SRS processes

The SRS images are acquired by using a home-built spectral-focusing hyperspectral SRS microscope system (Fig. S3 within the Supplemental Material) (for details refer to Sec. V of the Supplemental Material [29] and Ref.

[26]). The SRS system can be readily switched between fs excitation mode ($\tau = 100$ fs) and spectral focusing mode (ps excitation, $\tau = 1.8$ ps) by flipping the glass rods module out or into the SRS system. In this study, a DPBD crystal is synthesized as a bio-orthogonal Raman tag for SSRS imaging. The inset in Fig. 5(a) illustrates its chemical structure. DPBD shows a strong Raman peak at 2216 cm⁻¹, which is located in the silent region of Raman spectra of biological samples. Figures 5(a) and 5(c) show the measured SRS signals of DPBD crystals at 2216 cm⁻¹ vs $\sqrt{I_p I_S}$ and the geometric average of pulse energy in logarithmic scale under spectral focusing (ps excitation) and fs excitation modes, respectively. Theoretical study predicts that $\sqrt{I_p I_S} = 0.19$ TW/cm² and $\sqrt{I_p I_S} = 3.3$ TW/cm² are required for the saturation of SRS of DPBD by ps and fs excitations, respectively. (Refer to Sec. II A for the details of theoretical study and Sec. IV of the Supplemental Material for the related parameters of DPBD [29] and Refs. [39,40].) Compared with the reference line of unsaturated SRS $\sim I_p I_S$ with a slope of 2, the saturations of SRS signals (where the slope is <2) are observed, which coincide with theoretically predicted peak intensities for both ps and fs excitations. Similarly, Figs. 5(b) and 5(d) show the measured SRS of chloroplast in leaf sheath cells of rice at 1530 cm⁻¹. Saturations are observed with $\sqrt{I_p I_S}$ greater than 0.1 and 2 TW/cm², for ps and fs excitations, respectively. There are several Raman peaks involved in the measurements. In the spectral focusing case (ps excitation), the spectral resolution of our system is approximately 15 cm⁻¹, thus the Raman peaks of chlorophyll-*a* at 1530 cm⁻¹, chlorophyll-*b* at 1523 cm⁻¹ and chlorophyll-*d* at 1533 cm⁻¹ can be excited simultaneously [41]. In fs excitation, there should be more Raman peaks to be excited. To verify that the measured signal is due to the Raman effect, SRS images of DPBD in both resonant (2216 cm⁻¹) and nonresonant (2076 cm⁻¹) positions are displayed in Figs. 5(e) and 5(f). The intensity ratio of the selected areas is $I_{2076}/I_{2216} = 2\%$, which is close to the noise level, affirming that the measured signal is SRS. The transient absorption signal of chloroplast may contribute to the pump loss [42]. However, those pump-probe processes via electronic excited states largely happen in the visible region (450–700 nm) [42]. This is not the case for our current study as our pump wavelength is 898 nm. The SRS images of chloroplast in resonant (1530 cm⁻¹) and nonresonant (1590 cm⁻¹) modes [41] are also compared in Figs. 5(g) and 5(h). The intensity ratio of the selected areas is $I_{1590}/I_{1530} = 15\%$, indicating that SRS is the dominating process.

Comparing the results obtained by spectral focusing mode (ps) with those by fs excitation mode, the pulse energies required for saturation are similar (e.g., for DPBD it is about 0.6 nJ for both ps and fs excitations) [Figs. 5(a) and 5(c)], which are also in agreement with our theoretical calculations [0.63 nJ for ps excitations and 0.58 nJ for fs

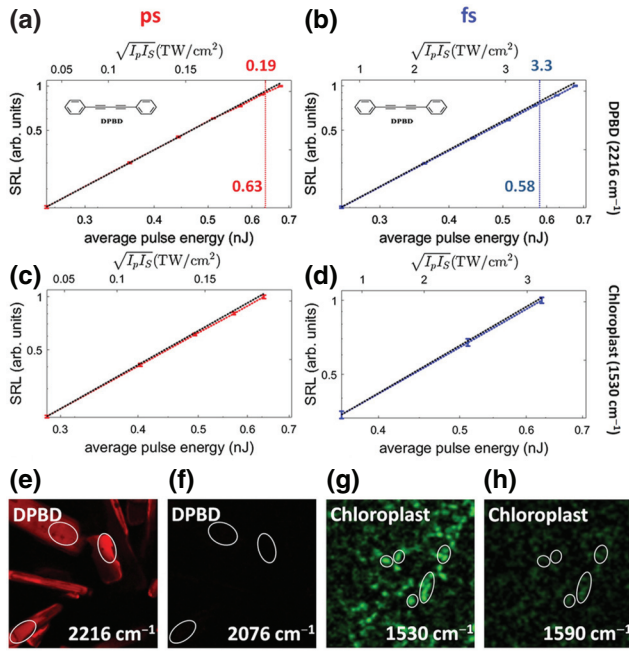


FIG. 5. Experimental observation of the saturation of SRS processes. (a),(b) Saturation of SRS for DPBD and chloroplast measured by spectral focusing mode (ps excitation). (c),(d) Saturation of SRS for DPBD and chloroplast measured by fs excitation mode. In each figure, the dotted black line is a reference line (i.e., unsaturated SRS signal), indicating the slope equal to 2. The red and blue data points stand for the SRS measured. The error bar indicates the standard error. The upper x axis stands for the geometric average of the peak intensity, while the lower x axis represents the geometric average of the pulse energy. (e),(f) SRS images of DPBD at 2216 cm^{-1} and 2076 cm^{-1} . (g),(h) SRS images of chloroplast at 1530 cm^{-1} and 1590 cm^{-1} . All SRS images are acquired by using the spectral focusing (ps) mode.

excitations, labeled in Figs. 5(a) and 5(c)]. Therefore, it is better to use the spectral focusing mode for SSRS imaging to avoid photodamage due to the high peak power of fs laser pulses. Note that in all of these SSRS experiments, SRL is measured under different Stokes powers, while the pump power is kept constant. To make sure that the measured saturation behavior is not due to photodamage and SRS measurements are repeatable, each curve is measured and repeated six times with standard errors of $<3\%$ (i.e., in the first, the third, and the fifth times, the Stokes power decreases from the maximum to zero step by step; meanwhile, the Stokes power increases from zero to the maximum in the second, fourth, and sixth measurements for SSRS measurements).

B. Enhancement of lateral and axial resolutions in SSRS imaging

We demonstrate the enhancement of both lateral and axial resolutions of the SSRS imaging technique by using DPBD crystals immersed in water. Figures 6(a) and

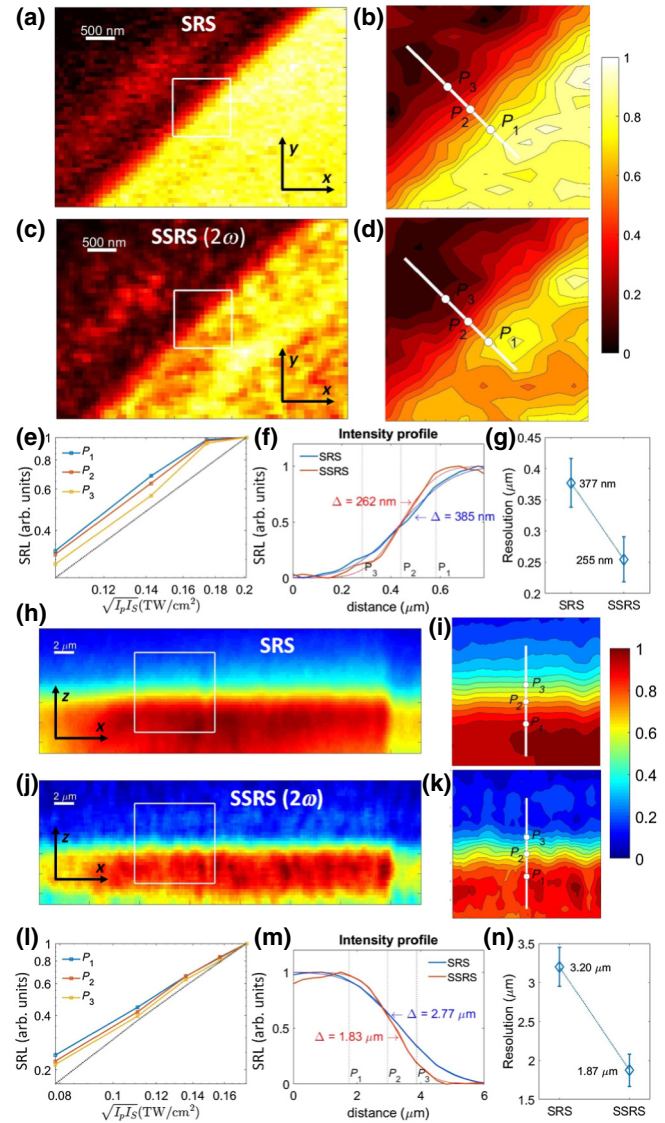


FIG. 6. Demonstration of both lateral and axial resolution enhancement by SSRS. (a),(h) SRS image of DPBD crystal immersed in water in the x - y plane and in the x - z plane. (c),(j) Corresponding second-order superresolution SSRS images. (b),(d),(i),(k) The contour plots of the selected area in (a), (c), (h), and (j), respectively. (e),(l) SRL vs $\sqrt{I_p I_s}$ at selected pixels P_1 , P_2 , and P_3 in (b) and (i), respectively. The dotted black line indicates slope equal to 2. (f),(m) The intensity profiles along the white line in (b) and (i), showing clearly resolution enhancement. The light-colored curves are the fitting results by error function. The resolution is indicated beside the curve. (g),(n) The average resolution measured at different locations of the interface between DPBD and water. The error bar stands for standard deviation. All the SRS and SSRS images are acquired by using the spectral focusing (ps) mode.

6(c) show the comparison of the conventional SRS and SSRS images along the x - y plane. The SSRS image is retrieved by the VSM method at the second-harmonic frequency (2ω). (Details refer to the VSM method in

Sec. II B.) Figures 6(b) and 6(d) show the corresponding contour plots of the selected areas in Figs. 6(a) and 6(c), respectively. Compared with a normal SRS image, the SSRS image provides a much sharper interface between water and DPBD crystals. Figure 6(e) gives SRL vs $\sqrt{I_p I_S}$ of selected pixels [labeled as P1, P2, and P3 in Figs. 6(b) and 6(d)] in logarithmic scale. The dotted black line is a reference line with a slope of 2, representing the conventional (unsaturated) SRS process. From P3 to P1, the slope is decreasing gradually, which means the level of saturation is increasing. The resolution enhancement comes from different levels of saturation. Figure 6(f) compares the intensity profiles along the white lines in Figs. 6(b) and 6(d).

To get a better understanding of spatial resolution enhancement in a quantitative way, the data is fit by error function [$h(x) = A_1 \int_{-\infty}^x \exp(-t^2/x_0^2) dt + A_2$], where A_1 , A_2 , and x_0 are fitting parameters. The fitting results are plotted as light-colored curves. The lateral resolution can be defined as the FWHM of the Gaussian function in the fitting function $h(x)$, that is, the resolution $\Delta = 2\sqrt{\ln 2}x_0$. This value is labeled beside the intensity profile. Then, the resolution is measured in this manner at nine different locations across the boundary of the sample. The average resolution and the standard deviation are plotted in Fig. 6(g). This shows that the lateral resolution is enhanced from 377 to 255 nm by a factor of 1.48, which is close to the theoretical value $\sqrt{2}$. (Refer to VSM method in Sec. I B.) In principle, the resolution enhancement of SSRS imaging is unlimited; however, in practical SSRS experiments, the extracted higher-order harmonic information of SSRS images could be limited by the shot-noise and the saturation levels due to the maximum excitation powers permitted without photodamaging the samples. The signal level at the second-harmonic order (2ω) is usually less than 10% of the control images and thus, the SSRS image has a relatively lower SNR. In our study, the signal of the third-harmonic order (3ω) is buried in noise.

To demonstrate the axial resolution enhancement by SSRS imaging, similar SSRS experiments are also conducted for the same DPBD sample. Figures 6(h) and 6(j) show the comparison of the conventional SRS and SSRS images along the x - z plane. The SSRS image is retrieved by the VSM method at the second-harmonic frequency (2ω). Figures 6(i) and 6(k) are the contour plots of the selected areas in Figs. 6(h) and 6(j). The interface between water and the DPBD crystal is much sharper in the SSRS image as well. Figures 6(l)–6(n) show a similar result to Figs. 6(e)–6(g). The axial resolution of SSRS imaging is enhanced by a factor of 1.71, which is slightly larger than the theoretical value $\sqrt{2}$. One notes that the $3 - \mu\text{m}$ -axial resolution is larger than the theoretical value approximately ($1 \mu\text{m}$), which is most probably due to the elongated point spread function arising from the

refractive index mismatch between water and the DPBD crystal in the SRS experiments [43].

C. Superresolution SSRS imaging for biological samples

We also apply the SSRS method for superresolution imaging of biological samples. Figures 7(a) and 7(b) show the comparison of label-free SRS and SSRS images of the chloroplast in leaf sheath cells of rice at 1530 cm^{-1} . Figures 7(c) and 7(d) show the enlarged images of the

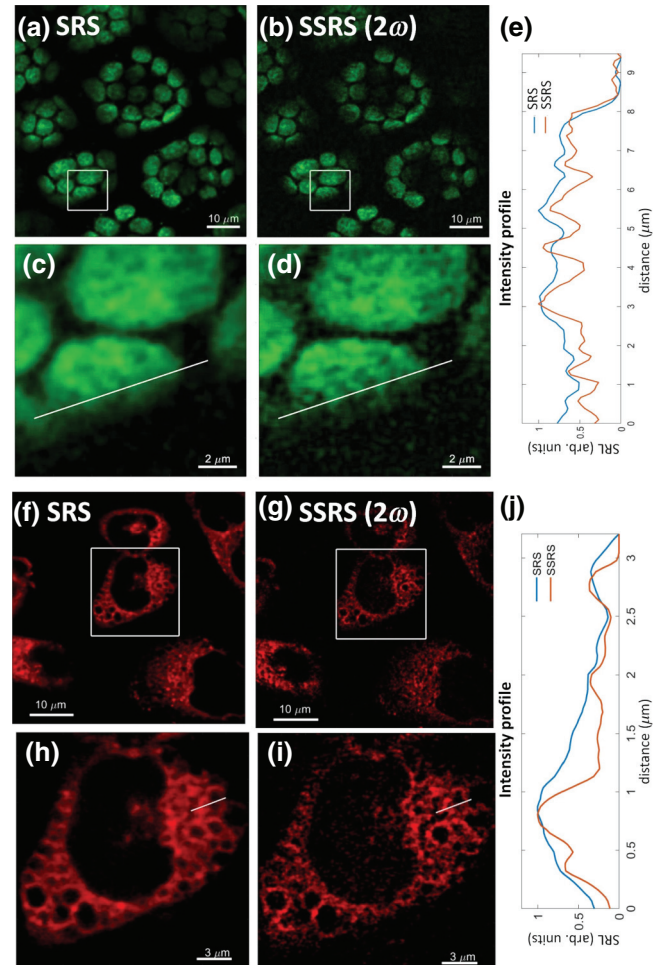


FIG. 7. Comparison of conventional SRS image and superresolution SSRS image of chloroplast and Raman-tagged mitochondria in live HeLa cells. (a),(b) SRS image and superresolution SSRS image of chloroplasts in leaf sheath cells of rice. The Raman shift is 1530 cm^{-1} . (c),(d) Enlarged SRS and SSRS images of the selected areas. (e) Intensity profiles across the lines indicated in (c) and (d). (f),(g) SRS image and second-order superresolution SSRS image of mitochondria in HeLa cells labeled with TPP-BDBPD. The Raman shift is 2216 cm^{-1} . (h) and (i) Enlarged SRS and SSRS images of the selected areas. (j), Intensity profiles across the lines indicated in (h) and (i). All the SRS and SSRS images are acquired by using the spectral focusing (ps) mode.

selected areas in Figs. 7(a) and 7(b). Apparently, the striped distribution of thylakoids can be found more clearly in the SSRS image [44]. The resolution enhancement can also be observed clearly through the intensity profiles shown in Fig. 7(e).

Mitochondria play a critical role in cell metabolism, including adenosine triphosphate production, apoptosis, and autophagy [45,46]. Superresolution fluorescence imaging of mitochondria is also reported to reveal interactions between cellular structures by STORM [47]. Compared with fluorescent imaging, Raman microscopy has a unique advantage in quantitative analysis. Alkyne-based Raman tag has been reported for SRS imaging of mitochondria [48]. In this SSRS study, we synthesize a Raman tag called TPP-BDBPD for mitochondrial targeting in which a DPBD molecule is modified to be BDBPD and connected with a TPP molecule. TPP is commonly used for mitochondria targeting [49]. The 2216 cm^{-1} Raman peak of DPBD is not affected by this connection in terms of both the Raman shift and the cross section. The SRS and SSRS images of mitochondria in Hela cells labeled with TPP-BDBPD are shown in Figs. 7(f) and 7(g), respectively. Figures 7(h) and 7(i) show the enlarged images of the selected areas in Figs. 7(f) and 7(g), respectively. The intensity profiles of the white lines are plotted in Fig. 7(j). SSRS images reveal a more detailed structure of a mitochondria network in cytoplasm [50]. Mitochondria are observed to undergo fusion and fission events continuously, resulting in a diverse range of the morphology of mitochondrial networks, which is related to numerous diseases (e.g., Parkinson, diabetes, cancer, and Alzheimer) [50]. The SSRS method in this work may provide alternative insights into the distribution of mitochondria in living cells with high spatial resolution.

IV. DISCUSSION

Different from fluorescence microscopy, SRS microscopy utilizing ultrafast lasers to excite the vibrations of inherent molecules provides a unique way to map biochemical distributions in living samples without the need of labeling, making SRS particularly suited for quantitative molecular imaging on biological and biomedical systems with high biochemical specificity and sensitivity. Although superresolution optical imaging to break the diffraction limit has been achieved for fluorescence microscopy, those superresolution techniques are challenging to directly apply to SRS microscopy. Our SSRS method to break the diffraction limit in this work has shifted conventional SRS imaging to the kingdom of superresolution. Superresolution SSRS imaging with the VSM method shares the same experimental set up as conventional SRS. Hence, SSRS can be readily applied to existing SRS microscopes as long as the excitation power is sufficient to achieve saturation without damaging the

samples. Our theoretical modeling on SSRS is not sample specific, thus theoretically, saturation of SRS can be observed in any sample. The resolution of SSRS imaging can be improved by extracting higher-order Fourier components with the VSM method. In principle, there is no limit of resolution enhancement by the SSRS technique. Hence, the SSRS technique holds promise as an appealing tool for superresolution SRS imaging in a variety of applications.

More generally, photon saturation is a versatile tool to improve spatial resolution in a variety of imaging modalities. There are typically two methods to achieve superresolution via saturation: (i) one can modulate the excitation beam by a sinusoidal function, then detect the harmonic modulation of the signal; (ii) besides normal excitation beams, another donut-shaped beam is used to saturate the signal from the rim part of the laser foci. Method (i) was first proposed in SAX [5] and has been applied for saturated two-photon fluorescence [51] and saturated CARS imaging [21]. Method (ii) is essentially a STED-like scheme, which has been applied for saturated pump-probe microscopy [52] and saturated fluorescent imaging [53]. Our VSM method is an alternative version of method (i). The sinusoidal modulation is implemented numerically in VSM. Compared to SAX, VSM can significantly reduce the dwell time for pulse laser excitation. To obtain a sinusoidally modulated intensity profile in the time domain, many pulses are needed in each modulation cycle. In this case, the dwell time has to be much longer than typical SRS imaging, in which there are only a few pulses in each modulation cycle. For example, in the SSRS image of chloroplast by VSM, the dwell time of a single image is $0.4\ \mu\text{s}$. Four images are acquired thus the total dwell time is $1.6\ \mu\text{s}$ only. In comparison, the dwell time in superresolution imaging of both saturated two-photon fluorescence and saturated CARS takes up to $100\ \mu\text{s}$ [21,51]. Methods like SAX by differential excitation, which is similar to VSM, can also be used to improve the detection efficiency [54]. The STED-like scheme of SSRS imaging is also feasible in principle. Although STED-like SSRS makes the set up more complicated, it is more suitable for fast SSRS imaging as it only needs to scan once to obtain a superresolution image; however, the VSM method requires scanning several times with different excitation powers for retrieval of a superresolution image.

In SSRS imaging, photodamage to the samples with high excitation power can be one of the main concerns. The damage threshold may vary from different samples under different imaging parameters (e.g., dwell time, averaging times, pixel size, etc.) [37,55]. In our mitochondria SSRS imaging under $I_p = 227\text{ GW/cm}^2$ and $I_S = 214\text{ GW/cm}^2$ with pixel dwell time of $2\ \mu\text{s}$ and averaged 40 times, photodamage is observed in approximately 15% of the cells, but no damage is observed if averaged <10 times. For chloroplast SSRS imaging under $I_p = 182\text{ GW/cm}^2$

and $I_S = 148 \text{ GW/cm}^2$ with $0.4 - \mu\text{s}$ dwell time without averaging, no obvious damage is observed. For SSRS imaging of DPBD crystals under $I_p = 208 \text{ GW/cm}^2$ and $I_S = 148 \text{ GW/cm}^2$ with $0.4 - \mu\text{s}$ dwell time without averaging, some parts could be damaged while some other areas are not. Compared to superresolution SSRS imaging with 75–150-nm pixel size, the saturation curves (Fig. 5) are measured with a $1.2 - \mu\text{m}$ pixel size and no photodamage is observed in all samples. Hence, the excitation power should be carefully controlled without damaging the samples for superresolution SSRS imaging.

It would be very attractive to apply the SSRS method for superresolution imaging of abundant biomolecules (e.g., lipids, proteins) in biological and biomedical samples. According to our theoretical modeling, saturation of C–H stretching in lipids and proteins requires a peak intensity of approximately 1 TW/cm^2 in the spectral-focusing mode, which is approximately fivefold higher than the maximum peak intensity available in our current SSRS set up. Since such a high excitation power is required for lipid and protein imaging, the photodamage effect should be assessed and controlled carefully [56]. In our SSRS HeLa cell imaging, the exposure time of one pixel is approximately $80 \mu\text{s}$ ($2 - \mu\text{s}$ dwell time, averaged 40 times). If the peak intensity increases by five times, the signal level will increase by 25 times while the shot noise will increase $\sqrt{5}$ times (in our cell imaging, the SRS signal level of the Raman tag used is comparable to the lipid and protein SRS signal). Hence, the SNR will increase by 11 times ($25/\sqrt{5}$). To maintain a similar SNR, the exposure time per pixel required is $80/11^2 \approx 0.66 \mu\text{s}$. Under such power levels, the photodamage is mainly due to energy transferred to the molecules through the SRS process [37]. The exposure time to induce photodamage is found to be inversely proportional to the square of the peak intensity [55], that is, if $80 - \mu\text{s}$ exposure time is acceptable for a 0.2 TW/cm^2 peak intensity, $80/5^2 = 3.2 - \mu\text{s}$ exposure time should be also acceptable while the peak intensity reaches 1 TW/cm^2 , as it is long enough to maintain the SNR. On the other hand, a lower repetition rate of laser sources can significantly reduce the risk of photodamage [37,55,56], thus a kHz laser would be a good option for superresolution SSRS imaging of lipids and proteins in biological samples, although sacrificing the imaging speed.

In summary, we demonstrate that the SSRS technique breaks the diffraction limit to enhance both the lateral and axial resolutions of SRS imaging in DPBD crystals, in which the VSM method is used to retrieve a superresolution SSRS image from a stack of SRS images acquired under different excitation powers. SSRS for superresolution imaging is proven for biological samples (e.g., chloroplast in leaf sheath cells, mitochondria in living HeLa cells labeled with TPP-BDBPD). The experimental observation is in agreement with the predicted SRS saturation peak

intensities in DPBD crystals for both ps and fs excitation. We expect that by choosing proper laser sources and adopting rapid scanning methods to mitigate any photodamage effect, the SSRS imaging technique promises to be an appealing tool for label-free far-field superresolution SRS imaging in biological and biomedical systems.

ACKNOWLEDGMENTS

This work was supported by the Academic Research Fund (AcRF)-Tier 1 and Tier 2 from Ministry of Education (MOE) (Grant No. MOE2014-T2-1-010), and the National Medical Research Council (NMRC) (Grant No. NMRC/TCR/016-NNI/2016), Singapore. The authors acknowledge Drs. Qing Shen and Naweed Isaak Naqvi in Temasek Lifesciences laboratory for providing us with the plant samples for SSRS imaging.

L. G. and Z. H. conceived the concept and designed the experiments. L. G., W. Z., and Z. H. wrote the manuscript. L. G. and W. Z. performed the experiments. Y. M. synthesized the Raman tag. Z. H. finalized the manuscript.

-
- [1] S. W. Hell and J. Wichmann, Breaking the diffraction resolution limit by stimulated emission: Stimulated-emission-depletion fluorescence microscopy, *Opt. Lett.* **19**, 780 (1994).
 - [2] M. J. Rust, M. Bates, and X. Zhuang, Sub-diffraction-limit imaging by stochastic optical reconstruction microscopy (STORM), *Nat. Methods* **3**, 793 (2006).
 - [3] E. Betzig, G. H. Patterson, R. Sougrat, O. W. Lindwasser, S. Olenych, J. S. Bonifacino, M. W. Davidson, J. Lippincott-Schwartz, and H. F. Hess, Imaging intracellular fluorescent proteins at nanometer resolution, *Science* **313**, 1642 (2006).
 - [4] M. G. L. Gustafsson, Surpassing the lateral resolution limit by a factor of two using structured illumination microscopy, *J. Microsc.* **198**, 82 (2000).
 - [5] K. Fujita, M. Kobayashi, S. Kawano, M. Yamanaka, and S. Kawata, High-Resolution Confocal Microscopy by Saturated Excitation of Fluorescence, *Phys. Rev. Lett.* **99**, 228105 (2007).
 - [6] J.-X. Cheng and X. S. Xie, Coherent anti-Stokes Raman scattering microscopy: Instrumentation, theory, and applications, *J. Phys. Chem. B* **108**, 827 (2003).
 - [7] C. W. Freudiger, W. Min, B. G. Saar, S. Lu, G. R. Holtom, C. He, J. C. Tsai, J. X. Kang, and X. S. Xie, Label-free biomedical imaging with high sensitivity by stimulated Raman scattering microscopy, *Science* **322**, 1857 (2008).
 - [8] K. Bae, W. Zheng, and Z. Huang, Quantitative assessment of spinal cord injury using circularly polarized coherent anti-Stokes Raman scattering microscopy, *Appl. Phys. Lett.* **111**, 063704 (2017).
 - [9] Z. Wang, W. Zheng, C.-Y. S. Hsu, and Z. Huang, Polarization-resolved hyperspectral stimulated Raman scattering microscopy for label-free biomolecular imaging of the tooth, *Appl. Phys. Lett.* **108**, 033701 (2016).

- [10] F. Lu, W. Zheng, and Z. Huang, Coherent anti-Stokes Raman scattering microscopy using tightly focused radially polarized light, *Opt. Lett.* **34**, 1870 (2009).
- [11] F. Lu, W. Zheng, C. Sheppard, and Z. Huang, Interferometric polarization coherent anti-Stokes Raman scattering (IP-CARS) microscopy, *Opt. Lett.* **33**, 602 (2008).
- [12] H. Yamakoshi, K. Dodo, A. Palonpon, J. Ando, K. Fujita, S. Kawata, and M. Sodeoka, Alkyne-tag Raman imaging for visualization of mobile small molecules in live cells, *J. Am. Chem. Soc.* **134**, 20681 (2012).
- [13] L. Wei, Z. Chen, L. Shi, R. Long, A. V. Anzalone, L. Zhang, F. Hu, R. Yuste, V. W. Cornish, and W. Min, Supermultiplex vibrational imaging, *Nature* **544**, 465 (2017).
- [14] W. P. Beeker, P. Groß, C. J. Lee, C. Cleff, H. L. Offerhaus, C. Fallnich, J. L. Herek, and K.-J. Boller, A route to sub-diffraction-limited CARS microscopy, *Opt. Express* **17**, 22632 (2009).
- [15] L. Gong and H. Wang, Breaking the diffraction limit by saturation in stimulated-Raman-scattering microscopy: A theoretical study, *Phys. Rev. A* **90**, 013818 (2014).
- [16] L. Gong and H. Wang, Suppression of stimulated Raman scattering by an electromagnetically-induced-transparency-like scheme and its application for super-resolution microscopy, *Phys. Rev. A* **92**, 023828 (2015).
- [17] W. R. Silva, C. T. Graefe, and R. R. Frontiera, Toward label-free super-resolution microscopy, *ACS Photonics* **3**, 79 (2016).
- [18] D. Kim, D. S. Choi, J. Kwon, S.-H. Shim, H. Rhee, and M. Cho, Selective suppression of stimulated Raman scattering with another competing stimulated Raman scattering, *J. Phys. Chem. Lett.* **8**, 6118 (2017).
- [19] D. S. Choi, B. J. Rao, D. Kim, S.-H. Shim, H. Rhee, and M. Cho, Selective suppression of CARS signal with three-beam competing stimulated Raman scattering processes, *Phys. Chem. Chem. Phys.* **20**, 17156 (2018).
- [20] B. J. Rao, D. S. Choi, and M. Cho, Selective suppression of CARS signal with two competing stimulated Raman scattering processes, *J. Chem. Phys.* **149**, 234202 (2018).
- [21] Y. Yonemaru, A. F. Palonpon, S. Kawano, N. I. Smith, S. Kawata, and K. Fujita, Super-Spatial- and -Spectral-Resolution in Vibrational Imaging via Saturated Coherent Anti-Stokes Raman Scattering, *Phys. Rev. Appl.* **4**, 014010 (2015).
- [22] H. Kim, G. W. Bryant, and S. J. Stranick, Superresolution four-wave mixing microscopy, *Opt. Express* **20**, 6042 (2012).
- [23] V. Raghunathan and E. O. Potma, Multiplicative and subtractive focal volume engineering in coherent Raman microscopy, *J. Opt. Soc. Am. A* **27**, 2365 (2010).
- [24] L. Gong, J. Lin, C. Hao, W. Zheng, S. Q. Y. Wu, J. Teng, C.-w. Qiu, and Z. Huang, Supercritical focusing coherent anti-Stokes Raman scattering microscopy for high-resolution vibrational imaging, *Opt. Lett.* **43**, 5615 (2018).
- [25] Y. Bi, C. Yang, Y. Chen, S. Yan, G. Yang, Y. Wu, G. Zhang, and P. Wang, Near-resonance enhanced label-free stimulated Raman scattering microscopy with spatial resolution near 130 nm, *Light: Sci. Appl.* **7**, 81 (2018).
- [26] K. Bae, W. Zheng, K. Lin, S. W. Lim, Y. K. Chong, C. Tang, N. K. King, C. B. Ti Ang, and Z. Huang, Epi-detected hyperspectral stimulated Raman scattering microscopy for label-free molecular subtyping of glioblastomas, *Anal. Chem.* **90**, 10249 (2018).
- [27] R. W. Boyd, *Nonlinear Optics* (Academic Press, Elsevier, Burlington, 2008), 3rd ed.
- [28] Y. Kawashima and G. Katagiri, Fundamentals, overtones, and combinations in the Raman spectrum of graphite, *Phys. Rev. B* **52**, 10053 (1995).
- [29] See Supplemental Material at <http://link.aps.org/supplemental/10.1103/PhysRevApplied.11.034041> for parameters used in the theoretical SSRS study, SVM method, synthesis and properties of the Raman tag, and the spectral focusing SRS imaging system.
- [30] E. F. d. Lima and J. E. M. Hornos, Matrix elements for the Morse potential under an external field, *J. Phys. B: At. Mol. Opt. Phys.* **38**, 815 (2005).
- [31] D. A. Long, *The Raman Effect: A Unified Treatment of the Theory of Raman Scattering by Molecules* (John Wiley & Sons Ltd, West Sussex, 2002).
- [32] W. P. Beeker, C. J. Lee, K. J. Boller, P. Groß, C. Cleff, C. Fallnich, H. L. Offerhaus, and J. L. Herek, A theoretical investigation of super-resolution CARS imaging via coherent and incoherent saturation of transitions, *J. Raman Spectrosc.* **42**, 1854 (2011).
- [33] C. Cleff, P. Groß, C. Fallnich, H. L. Offerhaus, J. L. Herek, K. Kruse, W. P. Beeker, C. J. Lee, and K.-J. Boller, Ground-state depletion for subdiffraction-limited spatial resolution in coherent anti-Stokes Raman scattering microscopy, *Phys. Rev. A* **86**, 023825 (2012).
- [34] C. Cleff, P. Groß, C. Fallnich, H. L. Offerhaus, J. L. Herek, K. Kruse, W. P. Beeker, C. J. Lee, and K.-J. Boller, Stimulated-emission pumping enabling sub-diffraction-limited spatial resolution in coherent anti-Stokes Raman scattering microscopy, *Phys. Rev. A* **87**, 033830 (2013).
- [35] M. R. Lewis, T. Marshall, E. H. Carnevale, F. S. Zimmoch, and G. W. Wares, Radiative lifetimes of excited electronic states in ionic species of nitrogen, *Phys. Rev.* **164**, 94 (1967).
- [36] E. J. Heilweil, R. R. Cavanagh, and J. C. Stephenson, Population relaxation of CO($v = 1$) vibrations in solution phase metal carbonyl complexes, *Chem. Phys. Lett.* **134**, 181 (1987).
- [37] H. Wang, Y. Fu, and J.-X. Cheng, Experimental observation and theoretical analysis of Raman resonance-enhanced photodamage in coherent anti-Stokes Raman scattering microscopy, *J. Opt. Soc. Am. B* **24**, 544 (2007).
- [38] O. Tzang, A. Pevzner, R. E. Marvel, R. F. Haglund, and O. Cheshnovsky, Super-resolution in label-free photomodulated reflectivity, *Nano Lett.* **15**, 1362 (2015).
- [39] Y. Kato and H. Takuma, Absolute measurement of Raman-scattering cross sections of liquids, *J. Opt. Soc. Am.* **61**, 347 (1971).
- [40] T. Etkorn, B. Klotz, S. Sørensen, I. V. Patroescu, I. Barnes, K. H. Becker, and U. Platt, Gas-phase absorption cross sections of 24 monocyclic aromatic hydrocarbons in the UV and IR spectral ranges, *Atmos. Environ.* **33**, 525 (1999).
- [41] Z.-L. Cai, H. Zeng, M. Chen, and A. W. D. Larkum, Raman spectroscopy of chlorophyll d from *Acaryochloris marina*, *Biochim. Biophys. Acta – Bioenerg.* **1556**, 89 (2002).

- [42] R. Berera, R. van Grondelle, and J. T. M. Kennis, Ultrafast transient absorption spectroscopy: Principles and application to photosynthetic systems, *Photosynth. Res.* **101**, 105 (2009).
- [43] J. Van der Kolk, A. C. Lesina, and L. Ramunno, Effects of refractive index mismatch on SRS and CARS microscopy, *Opt. Express* **24**, 25752 (2016).
- [44] V. Sarafis, Chloroplasts: A structural approach, *J. Plant Physiol.* **152**, 248 (1998).
- [45] M. T. Lin and M. F. Beal, Mitochondrial dysfunction and oxidative stress in neurodegenerative diseases, *Nature* **443**, 787 (2006).
- [46] R. Scherz-Shouval and Z. Elazar, ROS, mitochondria and the regulation of autophagy, *Trends Cell Biol.* **17**, 422 (2007).
- [47] B. Huang, S. A. Jones, B. Brandenburg, and X. Zhuang, Whole-cell 3D STORM reveals interactions between cellular structures with nanometer-scale resolution, *Nat. Methods* **5**, 1047 (2008).
- [48] X. Li, M. Jiang, J. W. Y. Lam, B. Z. Tang, and J. Y. Qu, Mitochondrial imaging with combined fluorescence and stimulated Raman scattering microscopy using a probe of the aggregation-induced emission characteristic, *J. Am. Chem. Soc.* **139**, 17022 (2017).
- [49] M. P. Murphy and R. A. J. Smith, Drug delivery to mitochondria: The key to mitochondrial medicine, *Adv. Drug Deliv. Rev.* **41**, 235 (2000).
- [50] H. Hoitzing, G. Johnston Iain, and S. Jones Nick, What is the function of mitochondrial networks? A theoretical assessment of hypotheses and proposal for future research, *BioEssays* **37**, 687 (2015).
- [51] R. Oketani, A. Doi, N. I. Smith, Y. Nawa, S. Kawata, and K. Fujita, Saturated two-photon excitation fluorescence microscopy with core-ring illumination, *Opt. Lett.* **42**, 571 (2017).
- [52] P. Wang, M. N. Slipchenko, J. Mitchell, C. Yang, E. O. Potma, X. Xu, and J.-X. Cheng, Far-field imaging of non-fluorescent species with subdiffraction resolution, *Nat. Photonics* **7**, 449 (2013).
- [53] G. Zhao, M. M. Kabir, K. C. Toussaint, C. Kuang, C. Zheng, Z. Yu, and X. Liu, Saturated absorption competition microscopy, *Optica* **4**, 633 (2017).
- [54] Y. Nawa, Y. Yonemaru, A. Kasai, R. Oketani, H. Hashimoto, N. I. Smith, and K. Fujita, Saturated excitation microscopy using differential excitation for efficient detection of nonlinear fluorescence signals, *APL Photonics* **3**, 080805 (2018).
- [55] Y. Fu, H. Wang, R. Shi, and J.-X. Cheng, Characterization of photodamage in coherent anti-Stokes Raman scattering microscopy, *Opt. Express* **14**, 3942 (2006).
- [56] K. König, T. W. Becker, P. Fischer, I. Riemann, and K. J. Halbhuber, Pulse-length dependence of cellular response to intense near-infrared laser pulses in multiphoton microscopes, *Opt. Lett.* **24**, 113 (1999).